CPFD Flow Pattern Simulation in Downer Reactors

Alireza Abbasi
Dept. of Chemical and Biochemical Engineering, The University of Western Ontario, London, ON, Canada

Reactech Process Development Inc., Markham, ON, Canada

Mohammad Ashraful Islam
Dept. of Chemical and Biochemical Engineering, The University of Western Ontario, London, ON, Canada

Paul E. Ege
Reactech Process Development Inc., Markham, ON, Canada

Hugo I. de Lasa
Dept. of Chemical and Biochemical Engineering, The University of Western Ontario, London, ON, Canada

DOI 10.1002/aic.13956
Published online November 26, 2012 in Wiley Online Library (wileyonlinelibrary.com).

This study contributes with a computational fluid dynamic simulation based on the numerical solution of continuity and momentum balance equations in a three-dimensional (3-D) framework. The proposed down flow gas–solid suspension model includes a unit configuration and C_D drag coefficients recommended for these units. Computational particle fluid dynamics (CPFD) calculations using suitable boundary conditions and a Barracuda (version: 14.5.2) software allow predicting local solid densification and asymmetric "wavy flows." In addition, this model forecasts for the conditions of this study higher particle velocity than gas velocity, once the flow reaches 1 m from the gas injector. These findings are accompanied with observations about the intrinsic rotational character of the flow. CPFD numerical 3-D calculations show that both gas and particle velocities involve the following: (a) an axial velocity component, (b) a radial velocity component (about 5% of axial velocity component), and (c) an angular velocity component. The calculated velocity components and the rotational flow pattern are established for a wide range of solid flux/gas flux ratios. © 2012 American Institute of Chemical Engineers *AIChE J,* 59: 1635–1647, 2013

Keywords: fluidization, down flow reactors, computational fluid dynamics, particulate systems, CREC-GS Optiprobes

Introduction

The characterization of flow patterns in downer reactors has progressed significantly in recent years.[1–2] A diversity of techniques have been applied to characterize both particle and gas flow in downer reactors.[1–8] In this respect, there have been significant advances in the development of fiber optic sensors and in the characterization of particle clusters.[3,4]

These downer reactors can be considered as displaying a relatively uniform flow structure and an expected plug-flow behavior for both gas and solid phases.[9] Due to low backmixing and short residence times, a downer reactor is suitable for the enhancement of a diversity of chemical processes such as the fluid catalytic cracking (FCC) process, residual oil cracking, and biomass and coal pyrolysis.[10,11] In this respect, it is essential to understand the macrostructural as well as the microstructural behaviors of the gas–solid flow in a downer reactor for reactor scale-up.[12]

The fluid dynamics in down flow reactors have been considered using a number of approaches. However, due to the complexity of bed down flow hydrodynamics, proposed approaches still show limitations.[13]

There are two types of theoretical approaches that one can use in computational fluid dynamics (CFD) to describe gas and solid flows: a continuum approach for both phases, which is known as Eulerian–Eulerian model or a continuum approach for the fluid and a discrete approach for particle phase also known as Eulerian–Lagrangian model.

In Eulerian–Eulerian model, solid phase is treated as a pseudofluid. The conservation equations for both phases are derived and correlated via constitutive relationships that obtained from empirical information and/or kinetic theory.[14,15] Eulerian–Eulerian model has been partially successful in simulating multiphase flow phenomena in risers in which gas and solids move concurrently upward.[8] This model, however, presents major limitations in describing the physical model of the gas–particle, particle–particle, and particle–wall interactions in the downer units.[8] Thus, the challenge is of providing closure equations for the averaged quantities. This closure becomes even more difficult to achieve for complex systems such as polydisperse solids.

On the other hand, discrete element method (DEM), based on Eulerian–Lagrangian approach, models the solid phase by tracking a finite number of discrete semirigid particles

Correspondence concerning this article should be addressed to H. I. de Lasa at hdelasa@eng.uwo.ca.

interacting through contact forces and transferring momentum to and from the fluid through a drag closure model. The advantage of this approach is that it can accommodate complexities such as polydispersity. DEM has, however, the disadvantage of (1) computational complexities when the particles population in the system surpasses a quantity (e.g., 2×10^5 particles) and (2) extensive computational time requirement even for the two-dimensional (2-D) solutions.[16] As a result, DEM shows limited abilities for relevant calculations in downer units either at the industrial or at laboratory-scale.

The computational particle fluid dynamics (CPFD) numerical scheme incorporates the multiphase-particle-in-cell (MP-PIC) method to describe solid phase. The MP-PIC method calculates the fluid phase using an Eulerian computational grid and the solid phase using Lagrangian computational particles. In MP-PIC, a particle stress gradient term is added to the equation of motion of particles. In the computation, the stress gradient on the grid is first calculated and then interpolated to discrete particles. In CPFD, a "numerical particle" is identified as an ensemble of particles with close properties such as species, size, and density.[17] The "numerical particle" provides a numerical approximation for the solid phase, similarly as the numerical control volume provides for the fluid phase, where its properties are considered essentially identical.

This work aims to describe downer hydrodynamics in three dimensions using the advanced CPFD method. This is the first Barracuda software application to downer units we are aware of. This approach allows describing particle motions and particle distributions providing snapshots along the downer unit. With this aim, the upcoming sections of this article will address various issues of modeling and simulation as follows: (a) "CPFD Mathematical Model" section considers specifically the proposed mathematical model as well as the selected boundary conditions, (b) the next section describes the configuration of the experimental setup as well as the selected dimensions and operating conditions, and (c) "Results and Discussion" section reports the CPFD simulations and includes a discussion of the various computational results obtained.

CPFD Mathematical Model

In CPFD simulation, the fluid phase is described as a continuum by solving the Navier–Stokes equations. On the other hand, the particle dispersed phase is treated by tracking a large finite number of particles through the calculated flow field (e.g., 10^5 particles). The momentum balance equations for the fluid phase can be derived from kinetic theory where the volume averaged fluid mass, momentum equations are defined as follows[18]

$$\frac{\partial}{\partial t}(\rho_f \theta_f) + \nabla \cdot (\rho_f \theta_f v_f) = 0 \tag{1}$$

$$\frac{\partial}{\partial t}(\rho_f \theta_f v_f) + \nabla \cdot (\rho_f \theta_f v_f v_f) = -\nabla P + \nabla \cdot \theta_f \tau_f + \rho_f \theta_f g - F \tag{2}$$

where θ_f is the fluid volume fraction, v_f is the fluid velocity, ρ_f is the fluid density, P is the fluid pressure, τ_f is the fluid stress tensor, and g is the gravitational acceleration. F represents the following average momentum exchange rate per volume between the fluid and particle phases as assess for the "numerical particle"

$$F = \iiint \varphi V_p \rho_p \left[\beta'(v_f - v_p) - \frac{\nabla P}{\rho_p} \right] dV_p d\rho_p dv_p \tag{3}$$

where ϕ is the particle probability function, V_p is the particle volume, ρ_p is the particle density, β' is the interphase drag coefficient, and v_p is the particle velocity.

The fluid stress tensor in Newtonian fluid is described as follows

$$\tau_{ij} = 2\mu_f S_{ij} - \frac{2}{3}\mu_f \delta_{ij} \frac{\partial u_i}{\partial u_j} \tag{4}$$

where μ_f is the fluid viscosity coefficient, S_{ij} is the rate of fluid deformation, and δ_{ij} is the Kronecker delta ($\delta_{ij} = 1$ if $i = j$ and $\delta_{ij} = 0$ if $i \neq j$). The rate of deformation, S_{ij}, defines the constitutive equation for the nonhydrostatic part of the stress as follows

$$S_{ij} = \frac{1}{2}\left(\frac{\partial u_i}{\partial x_j} + \frac{\partial u_j}{\partial x_i} \right) \tag{5}$$

The particle dispersed phase is governed by its respective mass and momentum conservation equations. The trajectory calculation of the discrete phase is made by integrating the force balance in particles. The particle motion is defined as proposed by Snider and Banerjee[18]

$$\frac{d}{dt}(v_p) = \beta'(v_f - v_p) - \frac{\nabla P}{\rho_p} - \frac{\nabla \tau_p}{\theta_p \rho_p} + g \tag{6}$$

where θ_p is the particle volume fraction, and τ_p is the particle normal stress. β', the interphase drag coefficient, is defined as follows

$$\beta' = C_d \frac{3}{8} \frac{\rho_f}{\rho_p} \frac{|v_f - v_p|}{\left(\frac{3V_{cluster}}{4\pi}\right)^{1/3}} \tag{7}$$

where C_d represents the drag coefficients and depends on the cluster Reynolds number.

$$C_d = \left(\frac{24}{ReK_1K_2} \left[1 + 0.1118(ReK_1K_2)^{0.6567} \right] + \frac{0.4305}{1 + \frac{3305}{ReK_1K_2}} \right) \theta_f^{-2.65} K_2 \tag{8}$$

$$Re = \frac{2\rho_f |v_f - v_p|}{\mu_f} \left(\frac{3V_{cluster}}{4\pi} \right)^{1/3} \tag{9}$$

$$K_1 = \frac{3}{1 + \frac{2}{\sqrt{\varphi}}} \tag{10}$$

$$K_2 = 10^{K_3} \tag{11}$$

$$K_3 = 1.8148(-\log\varphi)^{0.5743} \tag{12}$$

where $V_{cluster}$ is the particle cluster volume and φ is the sphericity defined as $N^{-1/3}$ with N representing the number of average particle size (volume weighted average) particles in a cluster.[5]

The modified drag coefficient proposed by Ganser,[19] including a volume fraction term, is the one considered in Eq. 8. The applicability of this type of correlation was suggested by Chhabra et al.[20] and Islam et al.[5] This correlation can be applied to a cluster-based drag coefficient and within a restricted range of Re ($4 < Re < 12$).[5] All Re for the conditions analyzed in this study remained in that range.

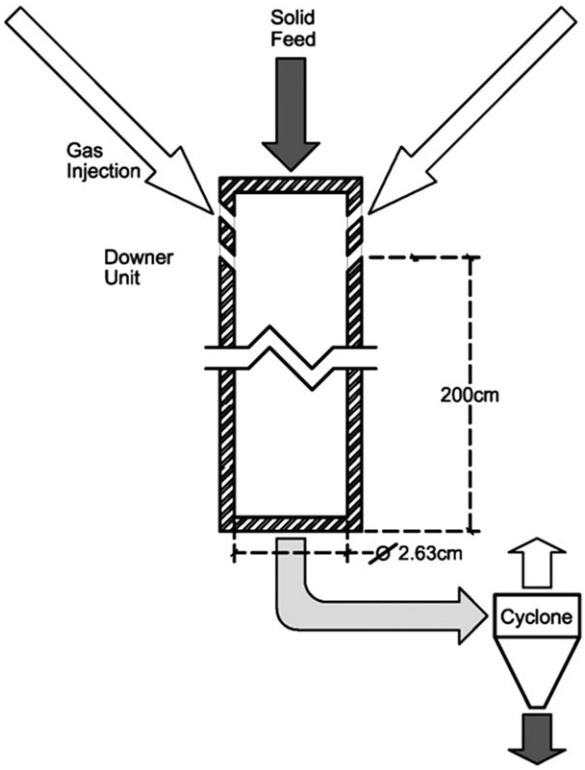

Figure 1. The schematic of the downer models.

In Eq. (13), τ_p represents the particle normal stress parameter for modeling particle collisions. This particle stress is derived from the particle volume fraction that is in turn calculated from particles mapped on a computational grid. Harris and Crighton[21] developed the continuum particle stress evaluating τ_p as follows

$$\tau_p = \frac{P_s \theta_P^{\beta}}{\max\left[\theta_{cp} - \theta_p, \varepsilon(1-\theta_p)\right]} \tag{13}$$

where P_s is a positive constant that has units of pressure, θ_p is solid volume fraction, and θ_{cp} is the particle volume fraction at close packing. ε and β are dimensionless constants. Recommended values for β are in the $2 \leq \beta \leq 5$ range.[22] The ε parameter is a small number in the order of 10^{-8} that is used to avoid singularity when the solid volume approaches closest packing.[22] The particle stress defined by Eq. 13 depends on the particle concentration and neglects the size and velocity of the particles influence. The ''anisotropy'' of components is accounted once, and Eq. 13 is used in the context of Eq. 6 yielding solid's velocity vector in various directions. The proposed particle normal stress model has been successfully used on each solid's velocity vector in modeling a large number of particles through the calculated flow field.[18] Solid collisions depend on solids concentration as well as on the deviation of solids velocity from a solids equilibrium velocity. The model applies the particle normal stress to a solid, up to the point where the solid reaches the particle-mean velocity.[18]

Regarding boundary conditions at the near wall, the turbulent gas velocity region is calculated using a 1/6 power function and a zero gas velocity at the wall surface. Concerning particle velocity, calculations includes Eq. 6 with wall and particle interactions assessed with both normal and tangential momentum restitution coefficients set at 0.95 (Table 2). These two restitution coefficients are selected as recommended by Zhao et al.[8]

In summary, the numerical method of this study is based on three-dimensional (3-D) Navier–Stokes equations for the fluid phase. The dynamic of the particle phase is described using the particle probability distribution function. Particle properties are interpolated to and from the Eulerian grid in the MP-PIC scheme. Interpolations are done using an interpolation operator and the product of interpolations in the three orthogonal directions.[18] This CPFD model is applicable to the fluid phase and to the particle phase. More specifically, this CPFD software is adequate, as it will be shown later to simulate fluid–particle and particle–particle interactions as pertinent in down flow reactors.

Experimental Setup, Simulation Parameters, and Verification of Numerical Procedures

Figures 1 and 2 provide a schematic diagram of a 2-m downer model with a 0.02632-m internal diameter used in the CREC laboratories for experimental fluid dynamic studies. A detailed description of the experimental unit is provided in Nova et al.[1] and Islam et al.[5,6] The downer air distributor is configured with sixteen 0.5-mm holes distributed evenly around the circumference of the column and angled downward 45° with respect to the vertical. These high-velocity jets intimately mix gas and solid particles.[5] This allows supporting the assumption of uniform solid and gas distribution at the downer entry, as adopted in the present model. The unit ends in a cyclone where gas and particles are separated. The downer unit as implemented in the CREC laboratories is provided with CREC Optiprobes allowing experimental characterization of gas–solid flow and measurements of particle clusters and solid densification.[6] To proceed with the simulations in the downer reactor, computational domains were established in the downer of Figure 1 using the following mesh: $7 \times 7 \times 557$ with these dimensions based on radial and axial dimensions, respectively. The adequacy of this grid configuration for both gas and solid phases was confirmed using different mesh sizes (e.g., all dimensions being double than in the $7 \times 7 \times 557$ grid). Deviations of calculated gas velocity, particle velocity, and solid values were smaller than 1%. Air and 84-μm FCC particles are fed from the top of the column via the feeding section as described in Figure 1.

Table 1 reports the various inlet air and particle fluxes, temperatures, and outlet parameters used in this simulation. Solid flows were selected in the simulation to represent an ample range of possible solid fluxes in downflow reactor units. Regarding solid particles, a typical FCC particle size distribution as shown in Figure 3, was considered in the simulation. The 14.5.2 release version of Barracuda software was used in the simulations.

The input parameters for the simulations are reported in Table 2. N_f represents the particle per unit volume or particle density in the feed. N_c represents the number of clouds. A ''cloud'' designates a large number of particles having the same attributes. The diffuse bounce, D_f, represents the random postcollision normal and tangential ''cloud'' velocities with the unit wall. This parameter emulates surface roughness effect.[15] Collisions of clouds with the walls are calculated using normal, e_n, and tangential, e_t, particle restitution coefficients. The values of restitution coefficients considered are the ones suggested by Zhao et al.[8] The ξ parameter represents an elastic restitution factor that limits the velocity of particles that bounce off of a region at close packing. The ς parameter represents the particle/fluid slip ratio at the cell

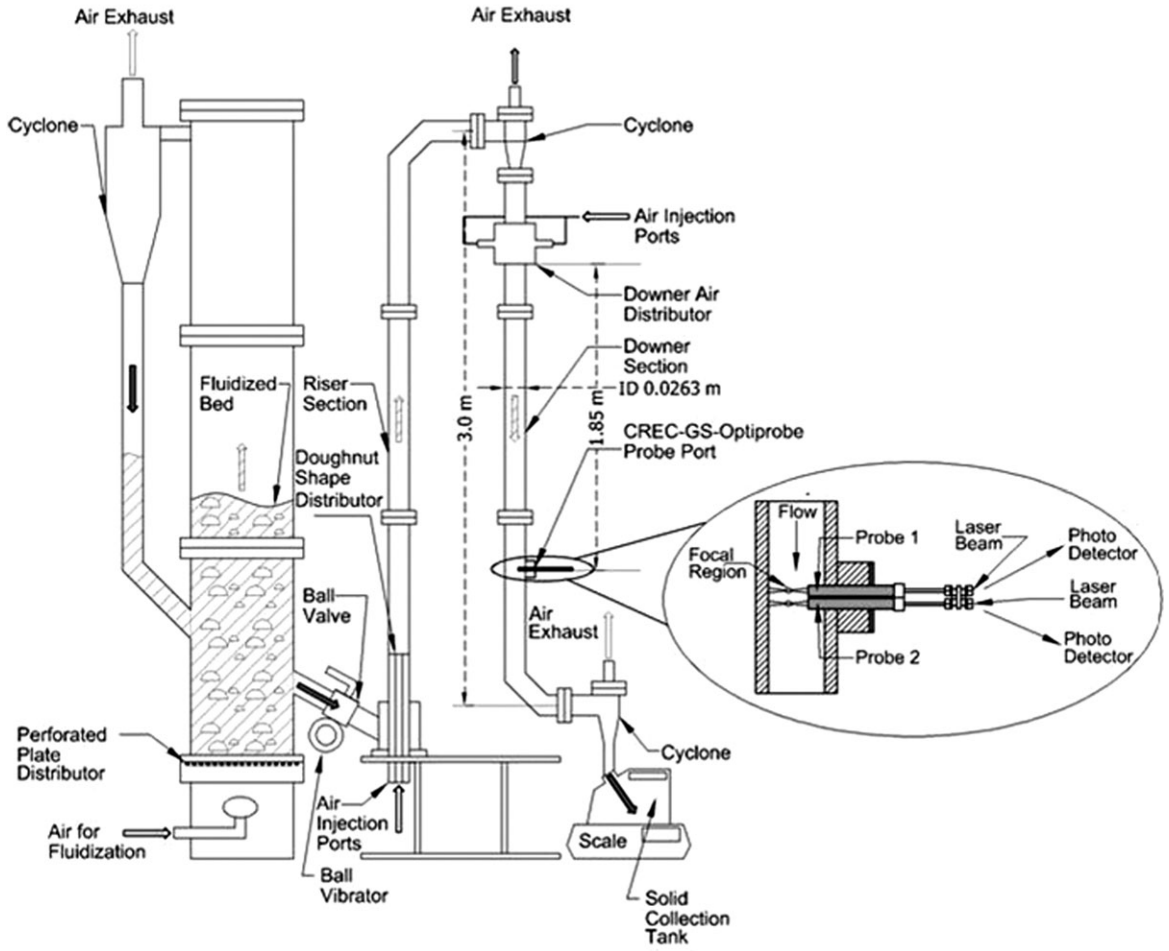

Figure 2. The experimental setup showing the general lay out of the downer unit available in CREC laboratories.

boundary with particle properties defined at the entry of cell where solids are being fed. β and P_s represent the dimensionless constants for the solid-phase stress model. These parameters are set at $\beta = 3$ and $P_s = 10$ Pa as recommended by Snider et al.[23]

The numerical solution of the linearized governing equations is performed using an iterative method. The iterations continue until a selected number of variables satisfy conditions assigned to the summation of residuals and until the maximum number of iterations (which in all cases have to be smaller than specified values) are reached. These computational control variables are as follows: (i) maximum iterations for volume calculations, I_v; (ii) residuals for volume, r_v; (iii) maximum iterations for pressure, I_P; (iv) residuals for pressure, r_P; (v) maximum iterations for velocity, I_u; and (vi) residuals for velocity, r_u.

The Δt incremental time involved in the computations has been limited, so that the gases or/and particles are not transported outside the selected calculations cell. Furthermore, to account for the convection flow effects, a turbulence model

Table 1. Simulation Parameter Values

Air (density 1.184 kg/m^3)	Mass fluxes
	Cases 1, 2, 3, 4 and 5: 2.25 kg/(m^2 s)
	Case 6: 1.12 kg/(m^2 s)
	Case 7: 2.19 kg/(m^2 s)
	Case 8: 2.26 kg/(m^2 s)
FCC particles (density 1722 kg/m^3)	Mass fluxes
	Case 1: 0.00 kg/(m^2 s)
	Case 2: 9.20 kg/(m^2 s)
	Case 3: 43.7 kg/(m^2 s)
	Case 4: 62.5 kg/(m^2 s)
	Case 5: 80.0 kg/(m^2 s)
	Case 6: 20.39 kg/(m^2 s)
	Case 7: 25.45 kg/(m^2 s)
	Case 8: 36.16 kg/(m^2 s)
Temperature	300 K
Outlet absolute pressure	0.11170 MPa

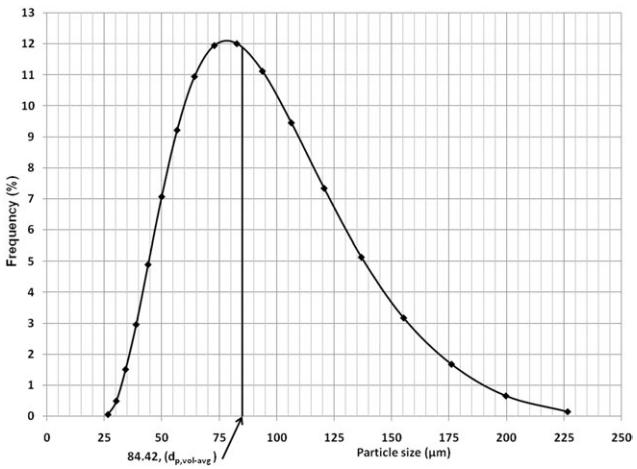

Figure 3. FCC particle size distribution.

Table 2. The Input Parameters for the Simulation

Time step, Δt	5×10^{-4} s
Particle–wall normal restitution coefficient, e_n	0.95
Particle–wall tangential restitution coefficient, e_t	0.95
Coefficient of contact friction, f_c	0.1
Diffuse bounce, D_f	0
Dimensionless constant of the solid-phase stress model, β	3
Dimensionless constant of the solid-phase stress model, ε	10^{-8}
Pressure constant of the solid-phase stress model, P_s	10 Pa
Solid volume fraction at closest packing, θ_{cp}	0.6
Gravitational acceleration, g	-9.8 m/s^2
Particle feed per average volume, N_f	300
Particle/fluid slip ratio, ς	1
Maximum volume iterations, I_v	1
Volume residual, r_v	10^{-6}
Maximum pressure iterations, I_P	2000
Pressure residual, r_P	10^{-8}
Maximum velocity iterations, I_u	50
Velocity residual, r_u	10^{-7}
Maximum momentum redirection from collision, ξ	40%
Total number of clouds, N_c	231,052

with a large eddy simulation is adopted using a quasisecond-order upwind scheme. This provides an accurate finite difference approach for the approximation of spatial derivatives.[24]

Preliminary work in this study involved the testing of the adequacy of numerical calculations. Figure 4 reports calculations of the particle mass flow at 2 m from the injection port and at the central position or at $r = 0$ m. One can see that in computational simulations at least 1.27 s is required for reaching a stable numerical value considered representative of the solid flow. From that point and on, the particle solid fluxes stay close to the stabilized average value as follows: 9.41 kg/(m^2 s) for Case 2, 43.66 kg/(m^2 s) for Case 3, 62.51 kg/(m^2 s) for Case 4, and 80.03 kg/(m^2 s) for Case 5. All these stabilized fluxes remain within a standard deviation of $\pm 5\%$. As a second step, to validate the numerical calculations, an additional confirmation of result adequacy for both satisfactory particle axial velocity and solid hold up was performed. This was done by using the following overall solid balance across the radius, for a time of observation of $\bar{\tau} = 8.73$ s at 2-m axial length in the downer

$$\frac{\rho_p}{R^2}\int_0^{\bar{\tau}}\left(\int_0^R v_{pz}(1-\theta_f)2r dr\right)dt \cong F_s\bar{t} \qquad (14)$$

It was observed that for all cases considered; the calculated and expected "$F_s\tau$" values (Eq. 14) deviated by less

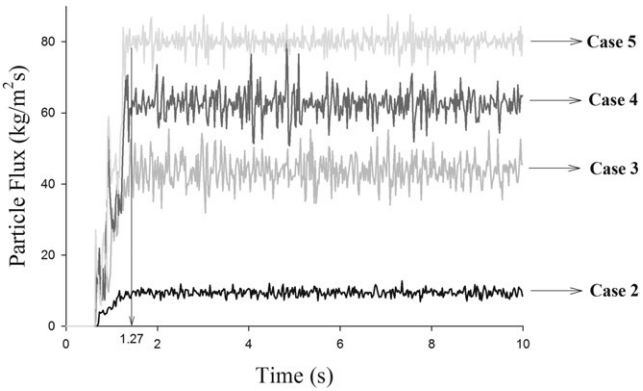

Figure 4. Average particle flux at 2 m from the gas injection port.

Operating conditions: 2.25 kg/(m^2 s) air flux and for Case 2: 9.20 kg/(m^2 s), Case 3: 43.7 kg/(m^2 s), Case 4: 62.5 kg/(m^2 s), and Case 5: 80.0 kg/(m^2 s) particle flux. The feeding temperature: 300 K.

than 1%. This was considered to be an excellent indicator of data consistency of the numerical results obtained.

Furthermore and as a third step of the numerical model validation, a specific comparison of experimental data and numerical results in downer units was developed as reported in Table 3. Experimental data were obtained from Islam et al.[5] These authors used a CREC Optiprobes located at the central position at 1.85 m down flow the gas feeding injection section. The CREC Optiprobe has the ability of measuring simultaneously particle cluster velocity, cluster size, cluster slip velocity, and local solid hold up. Given experimental data were available for a significant range of gas–solid fluxes from our own research group, these data were used for comparison with the numerical prediction of the same parameters.

With this end, four characteristic conditions involving clusters of 3–6 equivalent particle sizes were considered. The proposed comparison shows that for these four characteristic conditions the local averages of particle cluster velocity, cluster slip velocity, and local solid hold up are close with deviations in the $\pm 10\%$ range. Given the wide range of gas and solid fluxes considered, it was judged that the reported comparison provides adequate validation and support to the numerical model proposed in this study.

Results and Discussion

The computational fluid dynamic model for the downer reactor was established as adequate, given that predictions passed several numerical tests and given that there was favorable comparison with experimental data as described in the previous section. Based on these results, the model was

Table 3. Comparison of Simulated Particle, Gas and Slip Velocities As Well As Solid Holdup Values with Experimental Values Obtained using CREC-GS-Optiprobes

Number of Particles in Clusters	Solid Flux [kg/(m^2 s)]	Gas Flux [kg/(m^2 s)]	Slip Velocity (m/s)		Particle Velocity (m/s)		Gas Velocity (m/s)		Solid Holdup	
			Exp.	Num.	Exp.	Num.	Exp.	Num.	Exp.	Num.
$N = 3$	20.39	1.12	0.75	0.69 ± 0.13	1.796	1.744 ± 0.36	1.12	1.054 ± 0.15	0.0066	0.0058 ± 0.002
$N = 4$	43.7	2.25	1.06	0.99 ± 0.04	2.811	3.062 ± 0.05	2.25	2.072 ± 0.05	0.0090	0.0086 ± 0.003
$N = 5$	25.45	2.19	1.37	1.23 ± 0.12	3.277	3.428 ± 0.15	2.19	2.198 ± 0.11	0.0045	0.0049 ± 0.002
$N = 6$	36.16	2.26	1.50	1.42 ± 0.20	3.249	3.353 ± 0.17	2.26	2.115 ± 0.17	0.0065	0.0056 ± 0.002

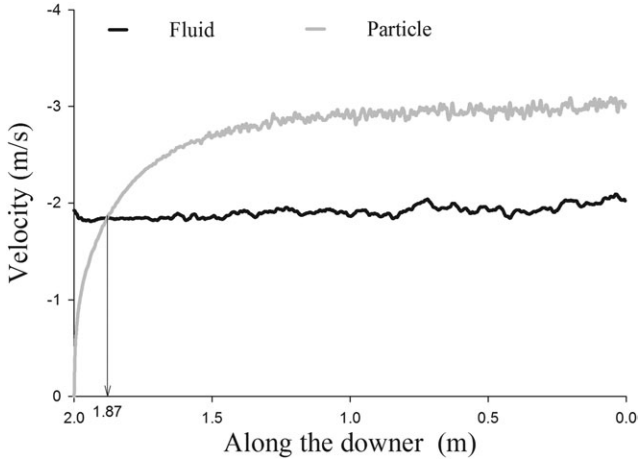

Figure 5. Average axial velocity profile along the downer.

Operating conditions: 2.25 kg/(m^2 s) air flux and 43.7 kg/(m^2 s) particle flux. The feeding temperature: 300 K.

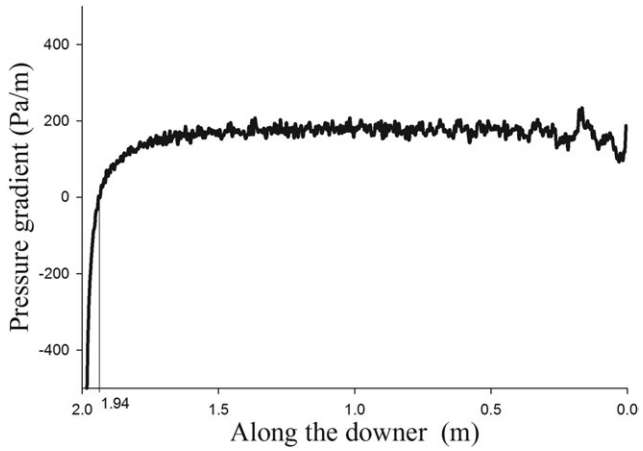

Figure 7. Average pressure gradient profile along the downer.

Operating conditions: 2.25 kg/(m^2 s) air flux and 43.7 kg/(m^2 s) particle flux. The feeding temperature: 300 K.

utilized extensively to provide macroscopic descriptions of the flow field as reported in Figures 5 and 6.

For instance, Figures 5 and 6 describe the average axial velocities for both gas and particles as well as for the pressure axial profile of 2.25 kg/(m^2 s) air flux and of 43.7 kg/(m^2 s) particle flux. The selected feeding temperature was 300 K, and the most probable cluster size assigned to this downflow solid suspension was $N = 4$ as shown in Table 3.

One can see that as anticipated, the cross-section average fluid gas velocity remained fairly constant along the downer. On the other hand, the average cross-section axial particle velocity goes from being smaller than the gas velocity at the injection port level and evolves toward superseding the gas velocity. This is expected given the influence of gravity exerted on the particles of the evolving gas–solid suspension. Toward the end of the downer, this velocity difference between phases or so-called slip velocity stabilizes and becomes particle or particle cluster terminal velocity.[5]

As reported in Figures 6 and 7, the proposed computational model yields an axial pressure profile that displays a quick pressure drop in the downer feeding section where particles are accelerated. This particle acceleration region is followed by a constant particle velocity section where there is a steady pressure increase. This is caused by the net effect of friction losses and hydrostatic pressure gains.

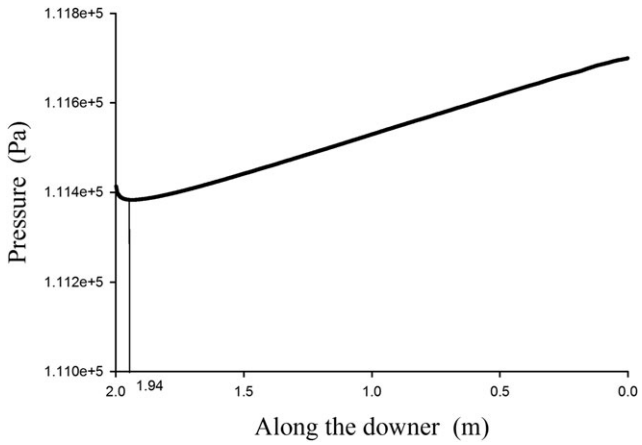

Figure 6. Average pressure profile along the downer.

Operating conditions: 2.25 kg/(m^2 s) air flux and 43.7 kg/(m^2 s) particle flux. The feeding temperature: 300 K.

These results are consistent with the ones observed by other researchers in the technical literature and provide in this respect, additional value to the model proposed.[25–29] Thus, on the basis of the above, one can conclude that the fluid dynamic cross-sectional average simulation results of the present computational model are consistent with the expected experimental fluid dynamic results in downer units (as already documented in the technical literature).

Furthermore, the proposed computational model can provide unique intrinsic 2-D and 3-D information. It is proposed in this study to fully exploit it to better understand the downer fluid dynamics. For instance, Figure 8 reports 2-D snapshots of the axial velocity profile for a 2.25 kg/(m^2 s) air flow and a 43.7 kg/(m^2 s) particle feed at various axial positions. One can observe that while in general, the same type of velocity profiles as in Figure 5 are obtained, there are intrinsic local and time-related variations in the properties of the described gas–particle suspension. These variations do not manifest while using simulated cross-sectional averaged properties. For instance, Figures 8a,b report gas and local particle velocities at various axial positions. It can be observed that both gas and particle velocities are reduced suddenly at one particular time and at a certain radial location. Without the 3-D-based time-dependent simulation, this variation might go unnoticed. Thus, Figure 8 shows that the downer fluid dynamic description (based on cross-sectional average axial particle and gas velocities, and cross-sectional average particle volume fractions), provides a macroscopic averaged representation but lacks the proper local and time-dependent details.

Figure 9 reports 3-D computational side-by-side snapshots at 2.25 kg/(m^2 s) air flux and 43.7 kg/(m^2 s) particle flux. In this figure, the gas and particle velocities are represented in separate 3-D plots. One can notice that there are moderate particle and gas velocity changes at different axial positions. Color codes change from light gray to black, with this change representing a typical standard deviation of 8 and 16% local and time-dependant particle and gas velocity variations, respectively.

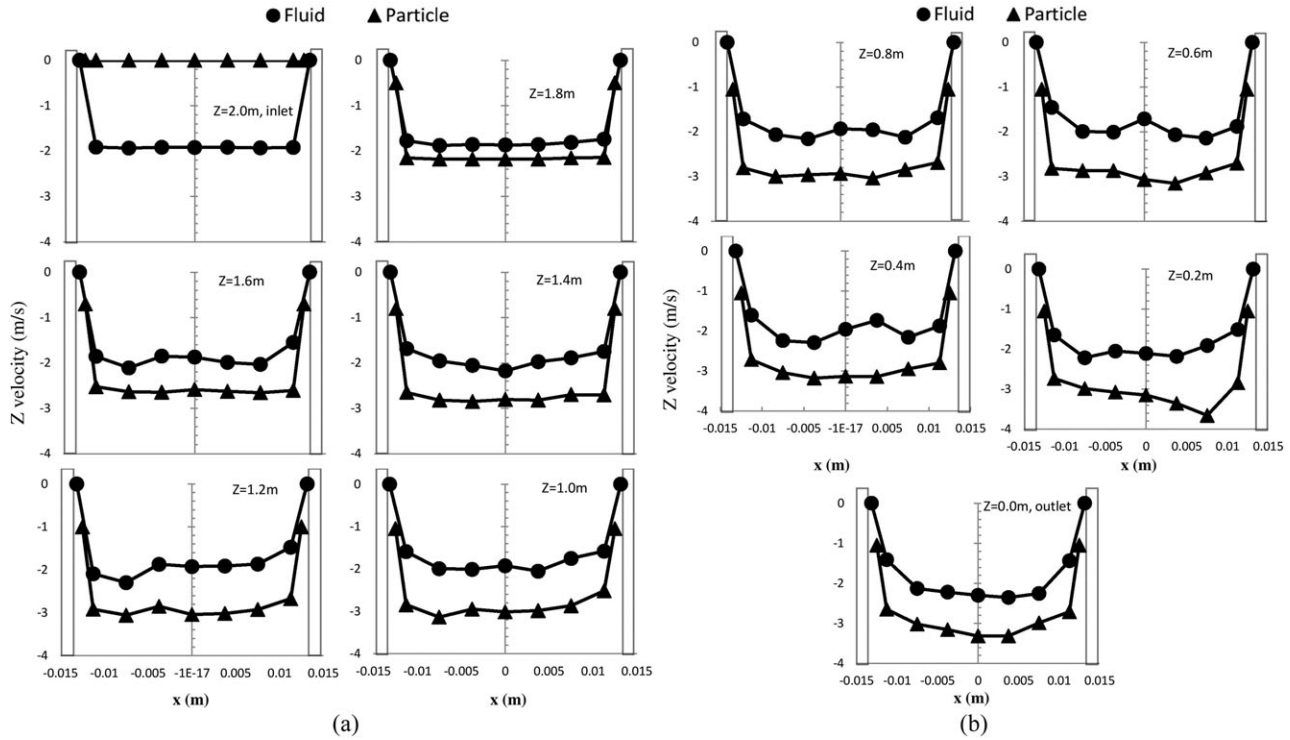

Figure 8. (a,b) Axial velocity profiles.

Operating conditions: 2.25 kg/(m^2 s) air flux and 43.7 kg/(m^2 s) particle flux. The feeding temperature: 300 K. Note: (a) axial levels from 2.0 to 1.0 m and (b) axial levels from 0.8 to 0 m.

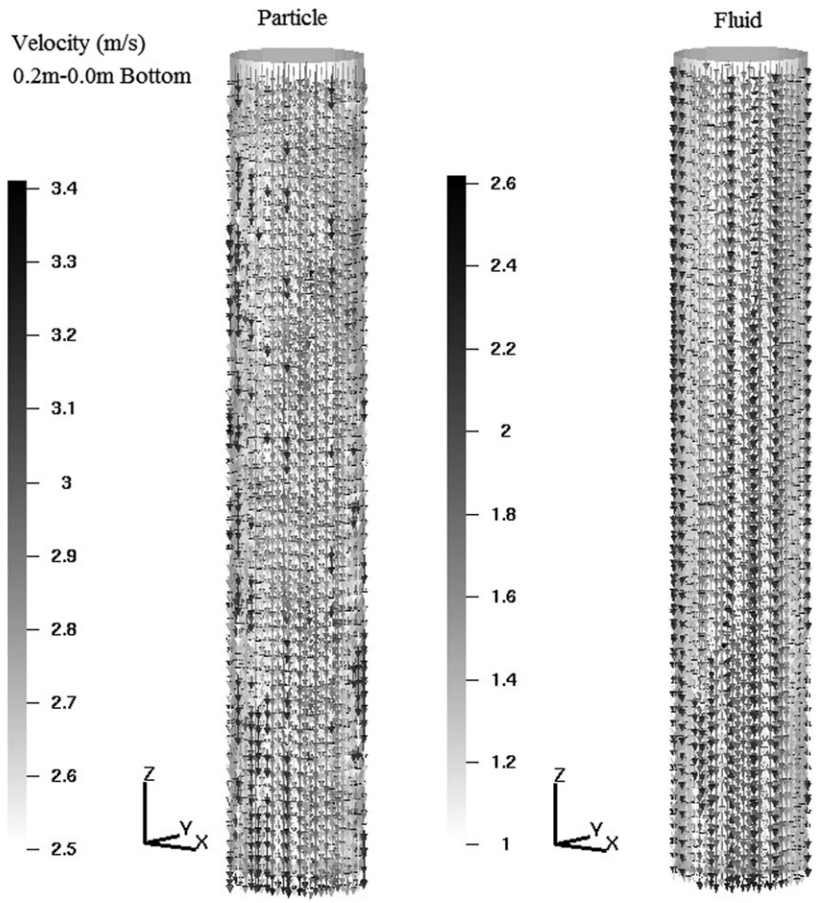

Figure 9. Particle and fluid overall velocity.

Operating conditions: 2.25 kg/(m^2 s) air flux and 43.7 kg/(m^2 s) particle flux. The feeding temperature: 300 K.

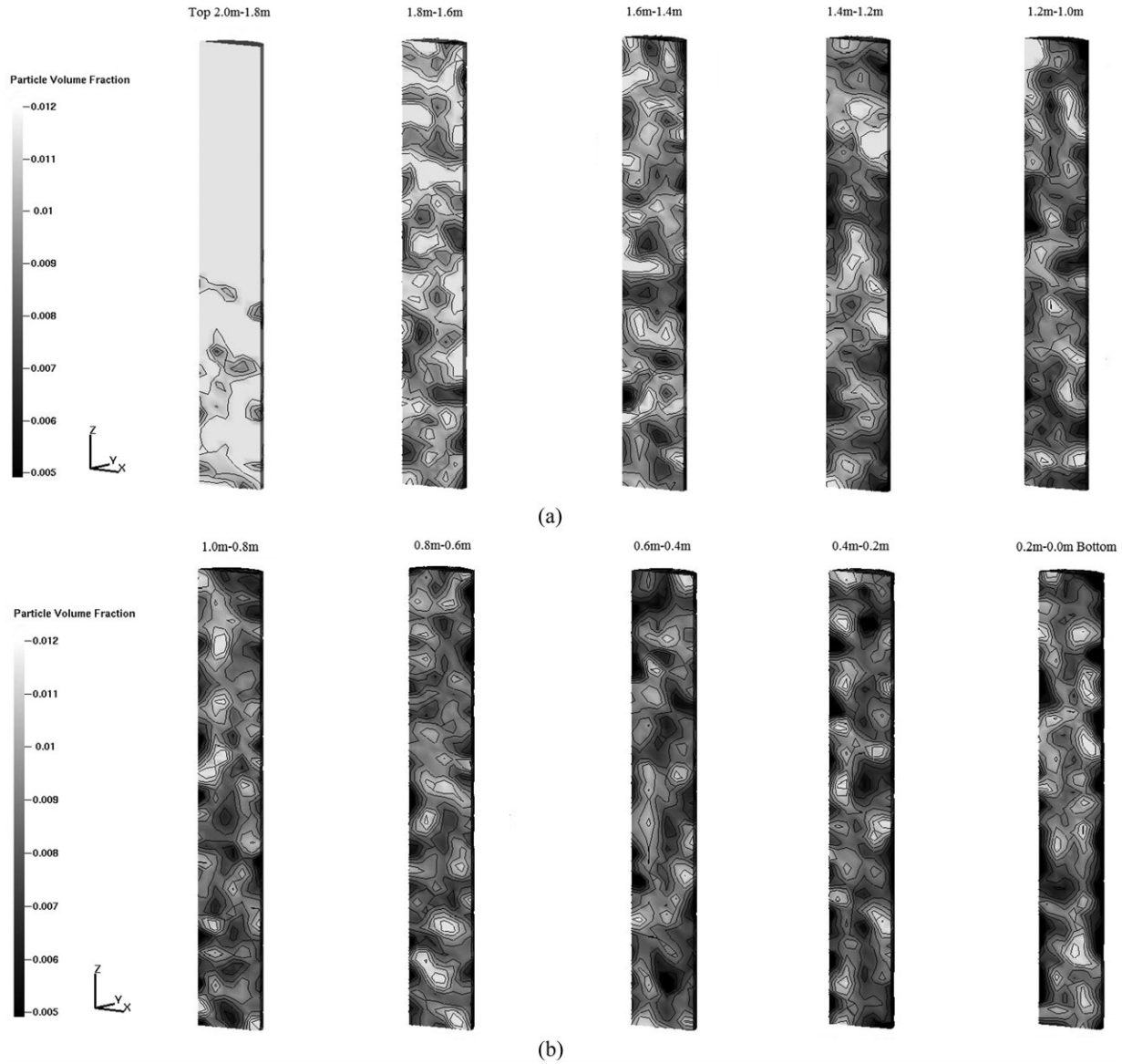

Figure 10. (a,b) Contour of particle volume fraction.

Operating conditions: 2.25 kg/(m^2 s) air flux and 43.75 kg/(m^2 s) particle feed. The feeding temperature: 300 K. Note: (a) axial levels from 2.0 to 1.0 m and (b) axial levels from 1 to 0 m.

Figure 9 also confirms the always concurrent changes of gas and particle velocity. For instance, when gas velocity increases particle velocity is augmented and when gas velocity decreases particle velocity is reduced. This manifests in fact, by an agreement of color codes representing both gas and particle velocities. In Figure 9, regions that are, for example, light gray in the left-hand side of the 3-D representation for particle velocity remain light gray in the right hand 3-D plot for gas velocity. Furthermore, and of special relevance is that both axial fluid and particle velocity change with radial position at various levels. One can see color codes changing from light gray to black at the same axial position. This means that at a given time and axial location, the velocities can change from about 1.0 to 2.6 m for fluid and 2.5 to 3.4 m/s for particles. In summary, a CPFD model using both 2- and 3-D plots becomes an essential and valuable tool to identify local and time-dependent fluid dynamic property changes. These changes are otherwise missed using experimental cross-sectional average property based downer simulation.

Figure 10 reports another interesting description of downer fluid dynamics, under the scope of the 3-D CPFD plots. This figure reports an axial cross-section snapshot of the downer column at various axial levels. Thus, it can be observed that there is a uniform downflow suspension flow close to the gas injection section. This flow becomes, however, progressive ''wavy'' with solid densification leading to regions of higher solid fraction followed by regions of lower solid fraction. This ''wavy'' flow becomes more apparent toward the end of the downer where the particle fraction variations are observed across the radial positions. One should note that these 3-D computational simulations are supported by downer suspension flow property variations as recorded by CREC Optiprobe sensors.[1,5] Nova et al.[1] and Islam et al.[5] measured ''particle clusters'' or solid densification evolving in the axial direction of the downer. Furthermore, these

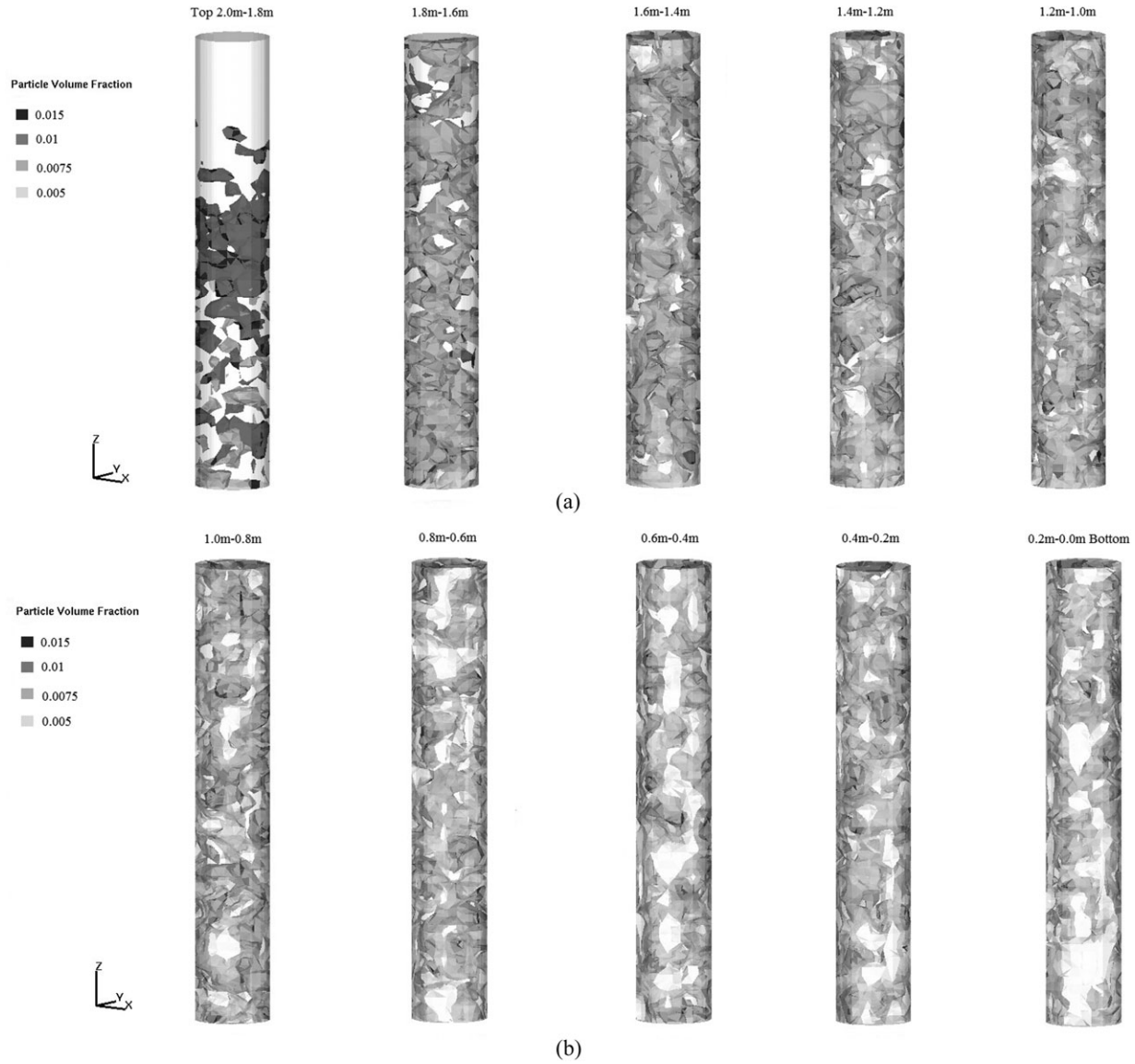

Figure 11. (a,b) Isosurface of particle volume fraction.

Operating conditions: 2.25 kg/(m^2 s) air flux and 43.75 kg/(m^2 s) particle feed. The feeding temperature: 300 K. Note: (a) axial levels from 2.0 to 1.0 m and (b) axial levels from 1 to 0 m.

observations are in agreement with CPFD 2-D fluid dynamic downer simulations as reported by Zhao et al.[8] They were able to describe densifications along the axial position in the downer under the constraints of the 2-D model.

Figure 11 illustrates 3-D particle fraction equiconcentration volumes. For instance, a volume enclosed by a light gray represents all solid fractions in this volume in the range of 0.01 and 0.015. Similar codes apply for the other enclosed volumes. As a result, this figure confirms a gas–solid downflow where one can observe well-distributed solid particles evolving toward a "wavy" flow with significant axial variation of particle concentrations. One can notice that the "wavy" flow becomes, at some point, asymmetric downstream, within the column. There are, in fact, in these regions not only particle densifications but also marked radial variations of particle concentration. This observation is consistent with Zhao et al.[8] who reported an asymmetric "wavy" flow in downers with particles moving literately from one wall to the other during their residence in the downer.

The CPFD simulation can also be used to provide snapshots of particle and gas velocities at various axial and radial downer locations. Figures 12 and 13 display these local properties for 2.25 kg/(m^2 s) air flux and 43.7 kg/(m^2 s) particle flux at a 300-K feeding temperature. One can see that there are correspondences of gas and particle velocity components. Both gas and particles display radial velocity vectors as described in Figures 12 and 13 These radial velocity components force the particle suspension not only to move downward but also circumferentially.

A rationalization of this downward and circumferential flow can be provided given the asymmetric "wavy flow" described in the previous sections of this article. Particle clusters move at a higher velocity than the gas. This tends to compress and redirect the gas toward regions of lower particle concentrations. This flow redirection generates radial fluid velocity components. Given the associated fluid drag on particles, radial gas velocity also imparts on particles radial velocity components. In this respect, one can see that

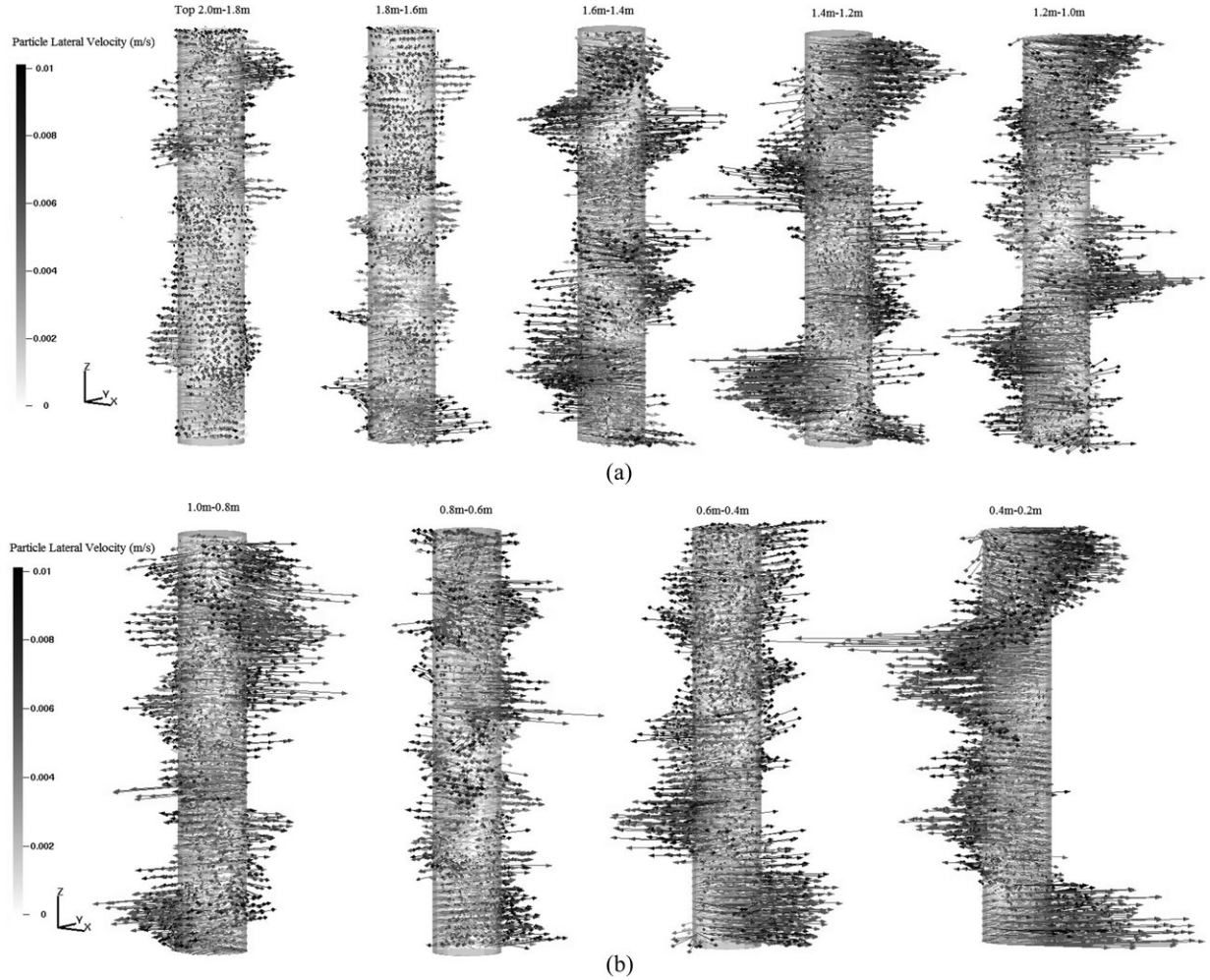

Figure 12. (a,b) Particle lateral velocity.

Operating conditions: 2.25 kg/(m^2 s) air flux and 43.75 kg/(m^2 s) particle flux. The feeding temperature: 300 K. Note: (a) axial levels from 2.0 to 1.0 m and (b) axial levels from 1 to 0 m.

local particle and gas velocities can display, as described in Figures 12 and 13, radial components of about 5–15% magnitude of the axial velocity component.

It appears that this promotion of circumferential flow is part of the intrinsic nature of a gas–solid downstream suspension. Fluid elements tend to be redirected toward regions of lower suspension density. It is also important to mention that this circumferential flow becomes increasingly important at lower axial positions. This progressively developing circumferential flow is consistent with the axial and radial variations of particle concentrations as reported in Figures 10 and 11.

Furthermore, in order to have confirmation of the gas–solid circumferential flow in the 3-D downer, additional simulations were developed as described in Figures 14 and 15. These figures focus on the downer outlet section located at 0.2–0 m axial position and on the following conditions: (a) 2.25 kg/(m^2 s) air flux and (b) 0, 9.2, 43.7, 62.5, and 80.0 kg/(m^2 s) particle flux.

One can observe that for 0 kg/(m^2 s) or for a down flowing of gas free of solid particles, there is no circumferential flow, with this being consistent with the expected classical single gas-phase fluid dynamics. However, as soon as the particle flow increases from 9 to 43.7 kg/(m^2 s), the circumferential flow gains importance. Finally, as soon as the solid flux surpasses the 43.7 kg/(m^2 s) level and moves up to 62.5 and 80.0 kg/(m^2 s), the circumferential flow is reduced in importance. Particle and gas radial velocities are then reduced to 4 and 2%, respectively, of the axial velocity values. Thus, it can be hypothesized that when at lower/moderate particle fluxes, the presence of solids and variation of suspension density promotes circumferential flow. It is also expected that this effect is reduced at higher solid fluxes. This dampening effect at higher solid fluxes can be assigned to the increasing influence of particle–particle interactions.

In summary, it is shown in this study that the CPFD simulation of the 3-D time-dependent gas–solid suspension in a downer becomes a valuable tool to identify essential features of the downer fluid dynamics. Examples of these features are ''wavy'' suspension and circumferential flow. It is anticipated that better understanding of 3-D downer fluid dynamics will facilitate downer scale-up and its extensive application for catalytic gas–solid reactions.

Conclusions

(a) The proposed gas–solid downer-based CPFD model complies with a series of numerical simulation stability, overall mass balance tests, and adequate simulation of experimental data in a downer unit.

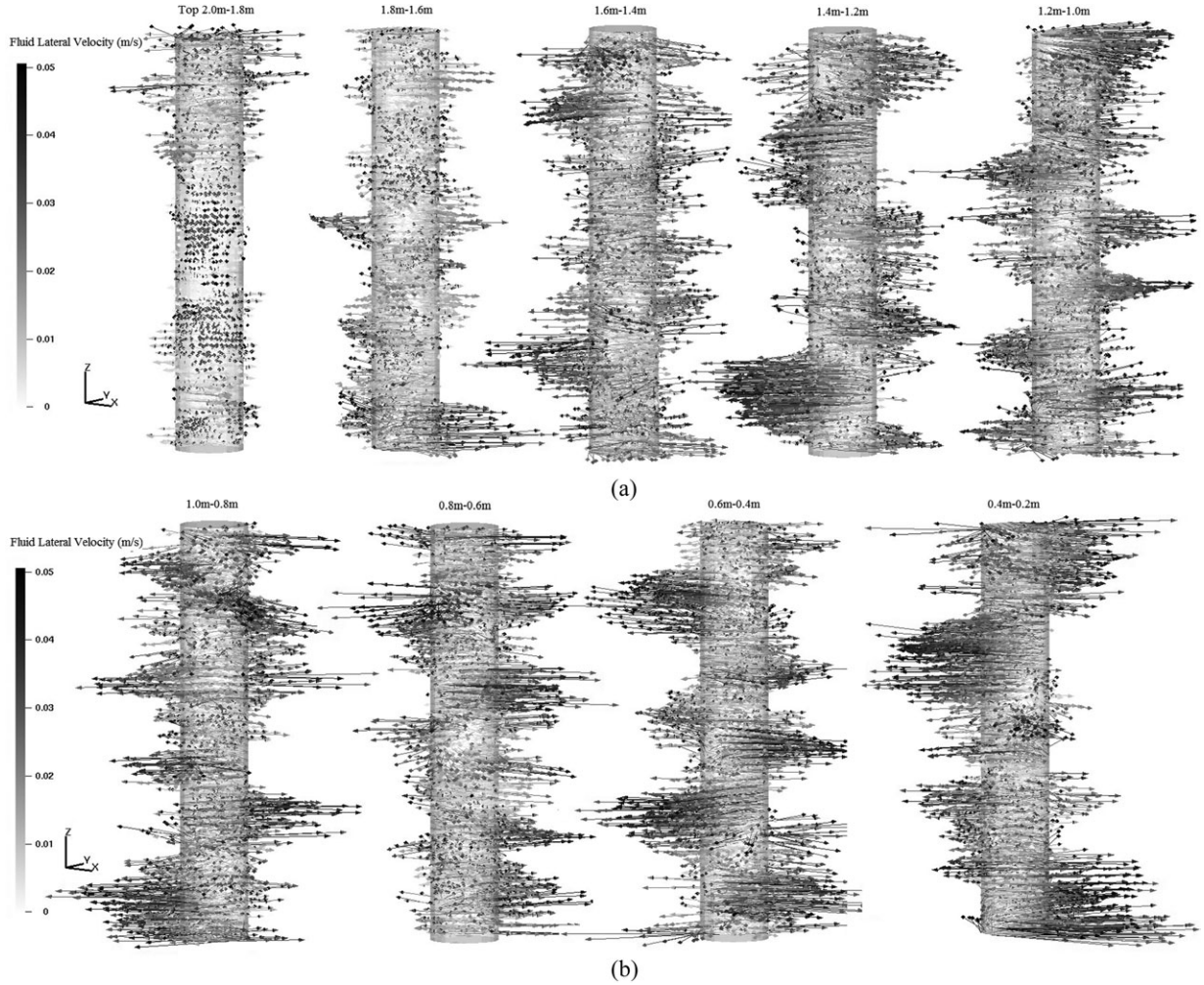

Figure 13. (a,b) Fluid lateral velocity.

Operating conditions: 2.25 kg/(m^2 s) air flux and 43.7 kg/(m^2 s) particle flux. The feeding temperature: 300 K. Note: (a) axial levels from 2.0 to 1.0 m and (b) axial levels from 1 to 0 m.

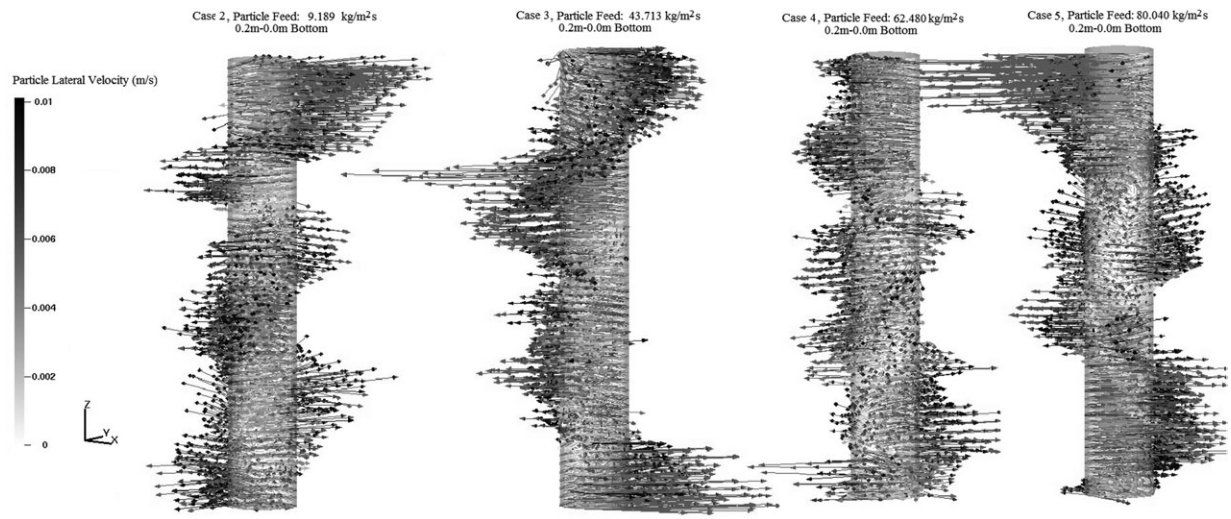

Figure 14. Comparison of particle lateral velocity at outlet.

Operating conditions: 2.25 kg/(m^2 s) air flux and for Case 2: 9.2 kg/(m^2 s), Case 3: 43.75 kg/(m^2 s), Case 4: 62.5 kg/(m^2 s), and Case 5: 80.0 kg/(m^2 s) particle flux. The feeding temperature: 300 K.

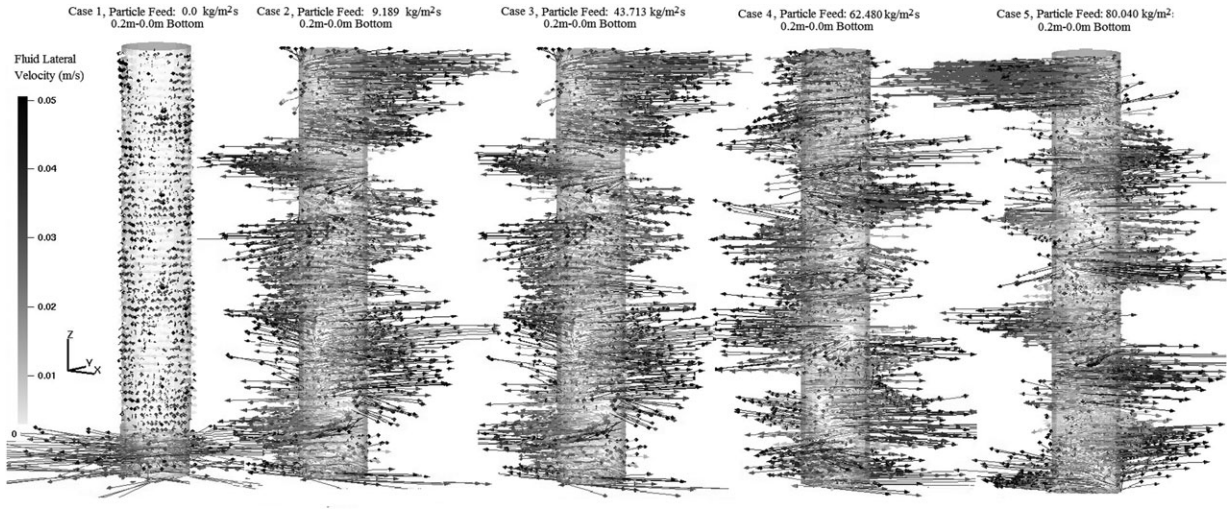

Figure 15. Comparison of fluid lateral velocity at outlet.

Operating conditions: 2.25 kg/(m^2 s) air flux and for Case 1: 0, kg/(m^2 s), Case 2: 9.2 kg/(m^2 s), Case 3: 43.72 kg/(m^2 s), Case 4: 62.5 kg/(m^2 s), and Case 5: 80.0 kg/(m^2 s) particle flux. The feeding temperature: 300 K.

(b) The 3-D downer simulations of this study are very valuable to describe the local and time variations of fluid dynamic properties in downers including particle/particle cluster velocities, gas velocity, and pressure.

(c) The 3-D simulations lead to the identification of particle clusters and an asymmetric ''wavy flow''. This asymmetric ''wavy flow'' promotes circumferential gas flow with radial velocity components for both the gas and the particles.

(d) The identified circumferential flow across solid fluxes leads to particles moving with radial velocity components. These radial velocity components are dampened, when solid particle concentrations reach higher particle concentrations.

Acknowledgments

The authors would like to acknowledge the financial contribution of the Natural Sciences and Engineering Research Council of Canada. The authors also like to thank the Mitacs program for the PDF Scholarship awarded to Dr. A. Abbasi. Authors would like to acknowledge Ms. F. de Lasa for her assistance on the preparation of this manuscript.

Notation

$A_{cluster}$ = particle cluster surface area, m^2
C_d = drag coefficient
dt = partial derivative of time, s
dr = partial derivative of radius, m
D_f = diffuse bounce
e_n = particle–wall normal restitution coefficient
e_t = particle–wall tangential restitution coefficient
F_s = solid mass flux, kg/(m^2 s)
f_c = coefficient of contact friction
F = momentum exchange rate per volume between the fluid and particle phase, N s/m^3
g = gravitational acceleration, m/s^2
I_P = maximum pressure iterations
I_u = maximum velocity iterations
I_v = maximum volume iterations
K_1 = function of sphericity
K_2 = function of sphericity
K_3 = function of sphericity
N = number of particles in a cluster
N_f = particle feed per average volume
N_c = total number of clouds
$\boldsymbol{P}$ = fluid pressure, N/m^2
P_s = positive constant, N/m^2
r = radius, m
r_P = pressure residuals
r_u = velocity residuals
r_v = volume residuals
$\boldsymbol{R}$ = radius of the downer, m
Re = Reynolds number
$V_{cluster}$ = particle cluster volume, m^3
V_p = particle volume, m^3

Greek letters

β = constant number
β' = interphase drag coefficient, 1/s
ς = particle/fluid slip ratio
ξ = maximum momentum redirection from collision
ε = constant number
ε_s = solid porosity
φ = cluster sphericity, $\frac{\pi^{\frac{1}{3}}(6V_{cluster})^{2/3}}{A_{cluster}}$
Δt = time step, s
μ_f = gas viscosity, N s/m^2
ρ_f = fluid density, kg/m^3
ρ_p = particle density, kg/m^3
θ_{cp} = particle volume fraction at close packing limit
θ_f = fluid volume fraction
θ_p = particle volume fraction
ϕ = particle probability function
τ_f = fluid stress tensor, N/m^2
τ_p = particle normal stress, N/m^2
$\bar{\tau}$ = time of observation, s
v_f = fluid velocity, m/s
v_p = particle velocity, m/s
v_{pz} = particle z velocity, m/s

Literature Cited

1. Nova SR, Krol S, deLasa H. Particle velocity and particle clustering in down-flow reactors. *Powder Technol*. 2004;148:172–185.
2. Luo B, Yan D, Ma YL, Barghi S, Zhu J. Characteristics of gas–solid mass transfer in a cocurrent downflow circulating fluidized bed reactor. *Chem Eng J*. 2007;132:9–15.
3. Qi XB, Zhang H, Zhu J. Solids concentration in the fully developed region of circulating fluidized bed reactor. *Powder Technol*. 2008; 183:417–425.
4. Vaishali S, Roy S, Mills PL. Hydrodynamic simulation of gas–solids down flow reactors. *Chem Eng Sci*. 2008;63:5107–5119.
5. Islam MA, Krol S, deLasa HI. Slip velocity in downer reactors: Drag coefficient and the influence of operational variables. *Ind Eng Chem Res*. 2010;49:6735–6744.
6. Islam MA, Krol S, deLasa HI. The CREC-GS-Optiprobes and its focal region: gas–solid flow measurements in down flow reactors. *Chem Eng Sci*. 2011;66:1671–1684.
7. Zhao T, Takei M. Discussion of the solids distribution behavior in a downer with new designed distributor based on concentration images

obtained by electrical capacitance tomography. *Powder Technol*. 2010;198:120–130.
8. Zhao Y, Ding Y, Wu C, Cheng Y. Numerical simulation of hydrodynamics in downers using a CFD-DEM coupled approach. *Powder Technol*. 2010;199:2–12.
9. Zhang H, Zhu J-X, Bergougnou MA. Hydrodynamics in downflow fluidized beds (1): solids concentration profiles and pressure gradient distributions. *Chem Eng Sci*. 1999;54:5461–5470.
10. Cheng Y, Wu C, Zhu J, Wei F, Jin Y. Downer reactor: from fundamental study to industrial application. *Powder Technol*. 2008;183:364–384.
11. Zhu J-X, Yu Z-Q, Jin Y, Grace JR, Issangya A. Cocurrent downflow circulating fluidized bed (downer) reactors—a state of the art review. *Can J Chem Eng*. 1995;73:662–677.
12. Lu X, Li S, Du L, Yao J, Lin W, Li H. Flow structures in the downer circulating fluidized bed. *Chem Eng J*. 2005;112:23–31.
13. Sunun L, Nattha T, Terdthai V, Parinya K. DEM modeling and simulation of a down-flow circulating fluidized bed. *Chem Eng Commun*. 2008;17:1328–1344.
14. Huilin L, Yurong H, Gidaspow D. Hydrodynamic modeling of binary mixture in a gas bubbling fluidized bed using the kinetic theory of granular flow. *Chem Eng Sci*. 2003;58:1197–1205.
15. Leboreiro J, Joseph GG, Hrenya CM, Snider DM, Banerjee SS, Galvin JE. The influence of binary drag laws on simulations of species segregation in gas-fluidized beds. Powder Technol. 2008;184(3): 275–290.
16. Snider DM, Clark SM, O'Rourke PJ. Eulerian–Lagrangian method for three-dimensional thermal reacting flow with application to coal gasifiers. *Chem Eng Sci*. 2011;66:1285–1295.
17. Snider DM. Three fundamental granular flow experiments and CPFD predictions. *Powder Technol*. 2007;176:36–46.
18. Snider DM, Banerjee S. Heterogeneous gas chemistry in the CPFD Eulerian–Lagrangian numerical scheme (ozone decomposition). *Powder Technol*. 2010;199:100–106.
19. Ganser GH. A rational approach to drag prediction of spherical and nonspherical particles. *Powder Technol*. 1993;77:143–152.
20. Chhabra RP, Agarwal L, Sinha NK. Drag on non-spherical particles: an evaluation of available methods. *Powder Technol*. 1999;101(3): 288–295.
21. Harris SE, Crighton DG. Solitons, solitary waves and voidage disturbances in gas-fluidized beds. *J Fluid Mech*. 1994;266:243–276.
22. Auzerais FM, Jackson R, Russel WB. The resolution of shocks and the effects of compressible sediments in transient settling. *J Fluid Mech*. 1988;195:437–462.
23. Snider DM, O'Rourke PJ, Andrews MJ, Sediment flow in inclined vessels calculated using a multiphase particle-in-cell model for dense particle flows. *Int J Multiphase Flow*. 1998;24: 1359–1382.
24. Amsden AA, Orourke PJ, Butler TD. *KIVA-II: A Computer Program for Chemically Reactive Flows with Sprays*. National Laboratory: Los Alamos, 1989.
25. Wang Z, Bai D, Jin Y. Hydrodynamics of cocurrent downflow circulating fluidized bed (CDCFB). *Powder Technol*. 1992;70: 271–275.
26. Tuzla K, Sharma AK, Chen JC, Schiewe T, Wirth KE, Molerus O. Transient dynamics of solid concentration in downer fluidized bed. *Powder Technol*. 1998;100:166–172.
27. Johnston PM, deLasa HI, Zhu J-X. Axial flow structure in the entrance region of a downer fluidized bed: effects of the distributor design. *Chem Eng Sci*. 1999;54:2161–2173.
28. Cao C, Weinstein H. Characterization of downflowing high velocity fluidized bed. *AIChE J*. 2000;46(3):515–522.
29. Bolkan Y, Berruti F, Zhu J, Milne B. Modeling circulating fluidized bed downers. *Powder Technol*. 2003;132:85–100.

Manuscript received Sept. 30, 2011, and revision received Sept. 18, 2012.